

EDGE ARTICLE

Cite this: *Chem. Sci.*, 2021, 12, 14773



All publication charges for this article have been paid for by the Royal Society of Chemistry

Received 28th July 2021
Accepted 13th October 2021

DOI: 10.1039/d1sc04124j

rsc.li/chemical-science

Type I macrophage activator photosensitizer against hypoxic tumors†

Guang Yang,‡ Song-Bo Lu,  ‡ Chong Li, Feng Chen, Jen-Shyang Ni, Menglei Zha, Yaxi Li, Ji Gao, Tianyi Kang, Chao Liu and Kai Li  *

Photodynamic immunotherapy has emerged as a promising strategy to treat cancer. However, the hypoxic nature of most solid tumors and notoriously immunosuppressive tumor microenvironment could greatly compromise the efficacy of photodynamic immunotherapy. To address this challenge, we rationally synthesized a type I photosensitizer of TPA-DCR nanoparticles (NPs) with aggregation-enhanced reactive oxygen species generation *via* an oxygen-independent pathway. We demonstrated that the free radicals produced by TPA-DCR NPs could reprogram M0 and M2 macrophages into an anti-tumor state, which is not restricted by the hypoxic conditions. The activated M1 macrophages could further induce the immunogenic cell death of cancer cells by secreting pro-inflammatory cytokines and phagocytosis. In addition, *in vivo* anti-tumor experiments revealed that the TPA-DCR NPs could further trigger tumor immune response by re-educating tumor-associated macrophages toward M1 phenotype and promoting T cell infiltration. Overall, this work demonstrates the design of type I organic photosensitizers and mechanistic investigation of their superior anti-tumor efficacy. The results will benefit the exploration of advanced strategies to regulate the tumor microenvironment for effective photodynamic immunotherapy against hypoxic tumors.

Introduction

Photodynamic immunotherapy is an emerging anti-cancer therapeutic strategy with low systemic toxicity and the absence of initial resistance, which harnesses the innate immune system to attack tumor cells.^{1–4} In general, the reactive oxygen species (ROS) that are generated during photodynamic therapy (PDT) can induce the immunogenic cell death (ICD) of tumor cells and activate the immune cells, triggering the immune response in the tumor microenvironment.^{5–8} However, the efficacy of photodynamic immunotherapy has always been limited by the harsh immunosuppressive nature of the tumor microenvironment. For instance, tumor-associated macrophage (TAM) is one of the critical drivers of an immunosuppressive tumor microenvironment, as it acts as a powerhouse for tumor angiogenesis and metastasis by secreting pro-tumor cytokines.^{9–14} In addition, the hypoxic conditions in solid tumors are another important restriction in realizing desired efficacy of photodynamic immunotherapy, because PDT processes are always oxygen-dependent and require oxygenated conditions.^{15–18} Therefore, there remains an urgent demand for

rationally designed photosensitizers, which can efficiently generate ROS under hypoxic conditions and induce the polarization of TAMs towards anti-tumor phenotypes (M1), to improve the outcome of advanced photodynamic immunotherapy.

Currently, it is still extremely challenging to overcome both immunosuppression and hypoxia in the tumor microenvironment using photodynamic immunotherapy, due to the lack of mechanistic understanding and shortage of strategic guidelines. The mechanism of PDT can be generally classified into two categories based on different photochemical reaction processes: type I and type II.^{19–23} In the type I pathway, hydrogen abstraction and electron transfer between photosensitizers (PSs) in the first excited triplet state (T_1) and biological substrates may occur to produce free radicals, which can interact with oxygen and water to produce superoxide anions ($^{\cdot}O_2^-$) and hydroxyl radicals ($^{\cdot}OH$), respectively.^{24–27} During the type II photochemical reaction, PSs in the T_1 state convert the surrounding 3O_2 into cytotoxic singlet oxygen (1O_2) *via* direct energy transfer.^{28,29} Therefore, type II PDT requires well-oxygenated environments, while type I PDT can be operated under hypoxic conditions for a broader range of application scenarios. Despite the successful commercialization of several organic PSs (*e.g.*, rose bengal and chlorin e6), most of the reported organic PSs generally favor type II PDT, because they do not possess the feature of inorganic counterparts that can facilitate the generation of electron–hole pairs to induce charge

Shenzhen Key Laboratory of Smart Healthcare Engineering, Department of Biomedical Engineering, Southern University of Science and Technology (SUSTech), Shenzhen 518055, China. E-mail: lik@sustech.edu.cn

† Electronic supplementary information (ESI) available. See DOI: 10.1039/d1sc04124j

‡ These authors contributed equally to the work.



separation as in the type I pathway.^{30,31} Therefore, the exploration of highly efficient organic type I PSs and elucidation of their working mechanism in hypoxic tumor environments will be of great benefit to the future development of photodynamic immunotherapy.

Herein, we have rationally designed and synthesized an aggregation-induced emission (AIE) photosensitizer, TPA-DCR, with a donor–acceptor (D–A) structure. The photosensitizer has shown aggregation-enhanced ROS generation upon light irradiation, mainly *via* the oxygen-independent type I mechanism. Theoretical calculation indicated that the small energy barrier between singlet and triplet states (ΔE_{ST}) may favor the formation of highly active T_3 and T_4 excitons in excited TPA-DCR molecules, thereby benefiting the electron transfer process to produce type I ROS. More importantly, we have demonstrated that the TPA-DCR nanoparticles (NPs) could effectively polarize the M0 and M2 macrophages toward the M1 phenotype under hypoxic conditions, leading to efficient killing of the 4T1 cancer cells through phagocytosis and secretion of pro-inflammatory cytokines. Interestingly, unlike traditional ICD caused by PDT, we discovered that the activated M1 macrophages could upregulate the expression levels of damage-associated molecular patterns (DAMPs) in 4T1 cells undergoing ICD. As a result, extensive *in vivo* experiments showed that our macrophage-mediated photodynamic immunotherapeutic strategy could induce the ICD of hypoxic tumor tissues and promote the infiltration of T cells, thereby significantly inhibiting tumor growth in a mice model.

Results and discussion

Synthesis and characterization of the photosensitizer

First, we designed and synthesized a donor–acceptor structured AIEgen, 2-(5-(4-(bis(phenyl)amino)benzylidene)-4-oxo-3-phenylthiazolidin-2-ylidene)malononitrile (TPA-DCR), in a one-step strategy. The structure of TPA-DCR was confirmed by molecular characterization in the ESI (Scheme S1 and Fig. S1–S3†). The photophysical results in tetrahydrofuran (THF) showed that TPA-DCR exhibited the main absorption and emission peaks at 460 nm and 608 nm, respectively (Fig. 1a). To better understand the photophysical properties of TPA-DCR, we carried out further theoretical calculation by using Gaussian 16 (ref. 32) with time-dependent density functional theory (TD-DFT) at the level of PBE1PBE/6-31G(d). The distribution of the lowest unoccupied molecular orbital (LUMO) and highest occupied molecular orbital (HOMO) of TPA-DCR in the S_1 state (Fig. 1b) indicated an energy gap of 2.24 eV. In addition, the excited geometries of TPA-DCR pointed to its twisted structure, having a dihedral angle of 1.87° between the hexatomic ring and five-membered ring (Fig. S4†). As an important indicator to evaluate the feasibility of the ISC process, the ΔE_{ST} values of TPA-DCR were calculated and are shown in Fig. 1c. The results indicated small ΔE_{ST} values (<0.3 eV) of TPA-DCR of S_1T_3 and S_1T_4 ISC channels. Based on Kohn–Sham frontier orbital analysis, the ISC process is more vulnerable to be triggered when the energy gap is below 0.3 eV.³³ As a result, the twisted structure of TPA-DCR can result in small ΔE_{ST} values in the excited state,

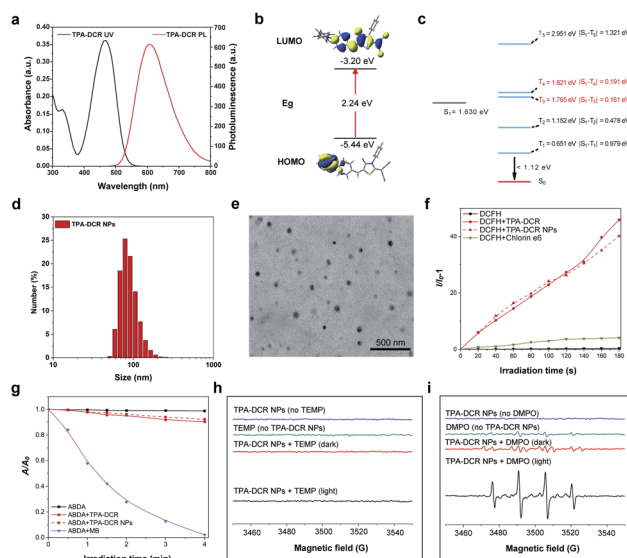


Fig. 1 (a) Ultraviolet-visible (UV-Vis) and photoluminescence (PL) spectra of TPA-DCR in THF. (b) The HOMO–LUMO distribution of TPA-DCR calculated by TD-DFT at the level of PBE1PBE/6-31G(d). (c) Relative energy levels of TPA-DCR calculated by TD-DFT. S_1 , S_0 and T_n represent the first-singlet, ground and multi-triplet states, respectively. (d) DLS and (e) TEM results of TPA-DCR NPs, and the scale bar is 500 nm. (f) Time-dependent changes of fluorescence intensities ($I/I_0 - 1$) at 525 nm for the DCFH indicator with TPA-DCR aggregates (90% PBS fraction in a PBS/THF mixture) and NPs, using the commercial photosensitizer chlorin e6 as a benchmark. (g) Time-dependent changes of absorption intensities (A/A_0) at 379 nm for ABDA mixed with methylene blue (MB), TPA-DCR aggregates (90% water fraction in a H_2O /THF mixture) and TPA-DCR NPs. EPR spectra of TPA-DCR NPs (1 mM) using (h) TEMP (100 mM) and (i) DMPO (100 mM) as the indicators. The white light irradiation of light-treated groups was conducted for 2 min at 40 mW cm^{-2} .

ensuring good ROS-generating ability. Especially, the ΔE_{ST} values of S_1T_3 and S_1T_4 channels are 0.191 eV and 0.161 eV, respectively. According to the literature, type I ROS can be generated after the occurrence of intersystem crossing (ISC) processes between S_1 and high-level triplet states.²⁰ Thus, the formation of highly active T_3 and T_4 excitons is promoted in excited TPA-DCR molecules, which might benefit electron transfer processes for type I ROS generation. In addition, the T_1 – S_0 energy gap of TPA-DCR is lower than the energy required to produce 1O_2 through excitation energy transfer (0.651 *versus* 1.12 eV).³⁴ Therefore, the type I mechanism dominates during the ROS generation of TPA-DCR.

The AIE characteristic of TPA-DCR was verified by measuring the fluorescence spectra in THF-water mixtures. The results indicated that TPA-DCR was faintly emissive with water fractions below 70%, while the emission intensity started to increase upon increasing the water fraction to 90% (Fig. S5†). However, TPA-DCR could barely produce ROS in THF solution with 0 vol% of PBS, but promoted ROS generation gradually with increased PBS fractions along with the formation of aggregates (Fig. S6†). To improve the biocompatibility of the photosensitizer for biomedical applications, TPA-DCR was further encapsulated in DSPE-PEG₂₀₀₀ to create water-

dispersible TPA-DCR NPs by nanoprecipitation following our established protocols.³⁵ The size and shape of these NPs were then measured using dynamic light scattering (DLS) and transmission electron microscopy (TEM). These NPs had an average hydrodynamic diameter of 80–90 nm with a spherical shape (Fig. 1d and e). The UV-Vis absorption and PL spectra of TPA-DCR NPs were similar to those of the THF solution (Fig. S7†). The time-resolved fluorescence spectra showed that the fluorescence lifetime of TPA-DCR aggregates ($\text{H}_2\text{O}/\text{THF} = 9/1$) and TPA-DCR NPs (in water) were 2.33 ns and 2.02 ns, respectively (Fig. S8†). The fluorescence quantum yield (QY) of TPA-DCR NPs was determined to be 29.3% using rhodamine B in ethanol (97%) as the standard (Fig. S9†),³⁶ suggesting their suitability in *in vivo* imaging evaluation.

After confirming the optical properties of TPA-DCR NPs, their total ROS, type II ROS and type I ROS production rates were then measured using the indicators of 2',7'-dichlorodihydrofluorescein (DCFH), 2,2'-(anthracene-9,10-diylbis(methylene))dimalonic acid (ABDA) and 3'-*p*-(hydroxyphenyl)fluorescein (HPF), respectively. The total ROS-generating rate from TPA-DCR NPs was ~10-fold that of the commercial photosensitizer of chlorin e6 (Fig. 1f). In contrast, the type II ROS produced under the same experimental conditions was only 10% of that generated from commercial methylene blue (MB, singlet oxygen quantum yield of 52%) (Fig. 1g). Meanwhile, TPA-DCR can generate a large number of free radicals upon light irradiation, using HPF as the indicator (Fig. S10†).^{37,38} We further characterized the *in vitro* ROS generation capability of the photosensitizer by electron paramagnetic resonance (EPR) spectroscopy, using 2,2,6,6-tetramethyl-4-piperidone (TEMP) and 5,5-dimethyl-1-pyrroline-*N*-oxide (DMPO) as spin-trap agents for $^1\text{O}_2$ and $\cdot\text{OH}$, respectively. As shown in Fig. 1h, the acquired EPR spectrum showed no signal in the presence of TEMP and TPA-DCR NPs under white light irradiation (40 mW cm^{-2}) for 2 min, indicating negligible generation of $^1\text{O}_2$ from the type II mechanism. On the other hand, the spectrum of DMPO + TPA-DCR NPs irradiated under white light for 2 min showed obvious EPR signals from the DMPO/ $\cdot\text{OH}$ adduct (Fig. 1i), displaying four-line resonances with 1 : 2 : 2 : 1 intensity (small fluctuations on the baseline indicate the signal of oxidized DMPO). Under both conditions, no obvious ROS signals could be observed in other control groups. These data suggested that the TPA-DCR NPs generated free radicals mainly *via* the type I PDT mechanism upon light irradiation, with negligible ability to produce singlet oxygen.

In vitro anti-tumor effect of activated macrophages

Prior to cell and animal experiments, the cytotoxicity of TPA-DCR NPs towards macrophages was first evaluated at varied concentrations on RAW264.7 cells using the CCK-8 assay. The results clearly indicated that TPA-DCR NPs had no significant light and dark cytotoxicity (Fig. S11†). In previous work, we designed an AIE photosensitizer that could efficiently activate macrophages by generating type I ROS.³⁹ Herein, we analyzed the macrophage activation by TPA-DCR NPs using ELISA (Fig. S12 and S13†), immunofluorescence staining (Fig. S14†)

and western blotting (Fig. S15†). In addition, we have examined the expression level of the pro-inflammatory cytokines of TNF- α from M0 and M2 macrophages treated with PBS, TPA-DCR NPs, PBS + light, and TPA-DCR NPs + light, showing significantly higher TNF- α expression (Fig. S16†). These data collectively confirmed that TPA-DCR NPs could polarize M0 and M2 macrophages to M1 phenotypes *via* activating the NF- κB signaling pathway.

Considering that most tumor microenvironments are hypoxic,^{40,41} we further investigated the validity and efficacy of our strategy to employ a type I photosensitizer for triggering macrophage activation under similar conditions. To establish the hypoxic environment during the polarization of M0 and M2 macrophages, the TPA-DCR NP-supplemented culture medium was charged with argon to expel oxygen before light irradiation. Therefore, the sample was under anaerobic conditions during the light irradiation for 3 min. After the light irradiation, the aerobic medium was replaced by a normal culture medium and the cells were cultured for 24 h under normoxic condition before ELISA analysis. The results showed that the efficacy of TPA-DCR NPs in activating M0 and M2 macrophages toward M1 remains consistent under hypoxic and aerobic conditions

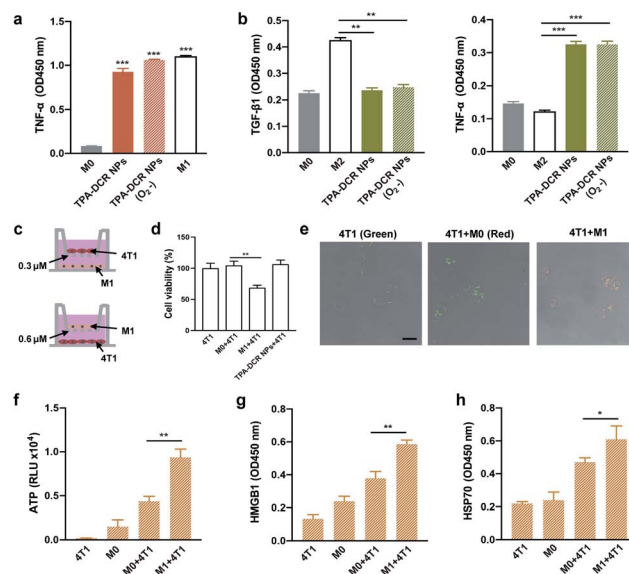


Fig. 2 (a) The level of proinflammatory cytokine TNF- α secreted by M0 macrophages upon activation by TPA-DCR NPs and light under aerobic or hypoxic conditions ($***p < 0.001$ vs. the M0 group, $n = 3$). (b) The level of anti-inflammatory cytokine TGF- $\beta 1$ and pro-inflammatory cytokine TNF- α secreted by M2 macrophages upon activation by TPA-DCR NPs and light under aerobic or hypoxic conditions, $**p < 0.01$, $***p < 0.001$ vs. the M2 group, and $n = 3$. (c) Schematic illustration of the transwell experimental procedures. (d) Cell viability of 4T1 cells treated with M0 macrophages, TPA-DCR NP-activated M1 macrophages or TPA-DCR NPs and light ($**p < 0.01$ vs. the M0 + 4T1 group, $n = 3$). (e) The phagocytosis effect of M1 macrophages on 4T1 cells as detected by confocal microscopy, and the scale bar is 25 μm . ELISA measurement of the expression levels of (f) ATP, (g) HMGB1 and (h) HSP70 in 4T1 cells treated with M0 macrophages or TPA-DCR NP-activated M1 macrophages ($*p < 0.05$, $**p < 0.01$ vs. the M0 + 4T1 group, and $n = 3$). The concentration of TPA-DCR NPs is 50 μM , and white light irradiation is set to be 10 mW cm^{-2} for 3 min.

(Fig. 2a, b and S17†), suggesting that the TPA-DCR NPs are not oxygen-dependent owing to their type I PDT signature.

In order to further verify the effectiveness of activated M1 macrophages in killing tumor cells, transwell chambers (0.3 μm), which only allow cytokines to pass (Fig. 2c), were used to analyze the anti-tumor effect of pro-inflammatory cytokines produced by M1 macrophages. First, RAW264.7 cells were added in the lower layer after being treated with TPA-DCR NPs and light (10 mW^{-2} white light, 3 min) for activation. The 4T1 cells were subsequently added to the upper layer of M0 (RAW264.7), M1 macrophages (RAW264.7 pre-treated with TPA-DCR NPs and light for polarization), and only TPA-DCR NPs. The cell viability of 4T1 cells was subsequently measured by CCK-8 after 24 h. The results indicate that $\sim 40\%$ of the 4T1 cells in the upper layer were killed by soluble factors (including pro-inflammatory cytokines) secreted by the activated macrophages. But there was no death in 4T1 cells treated with only M0 macrophages or those treated with TPA-DCR NPs + light irradiation in the absence of macrophages (Fig. 2d). Then, we chose transwell chambers with a larger pore size (0.6 μm , allowing cells to pass) to verify whether the TPA-DCR NP-activated macrophages could phagocytize 4T1 cells. To facilitate the study of cellular interactions, the 4T1 cells were prelabeled with a green-emissive fluorophore BTPETD, while M0 or M1 macrophages were prelabeled with a red-emissive fluorophore TPET-PAFN.⁴² The 4T1 cells were added to the lower layer while M0 and M1 macrophages (RAW264.7 pre-treated with TPA-DCR NPs) or a blank sample was added to the upper layer. After 24 h, the cells in the lower layer from all three groups were imaged under a confocal microscope. Fluorescence imaging results indicated that M1 macrophages could phagocytize 4T1 cells with a clear overlay of red and green fluorescence signals. On the other hand, only green fluorescence from 4T1 cells could be observed in the other two groups (4T1 and 4T1 + M0), suggesting that the absence of phagocytosis by macrophages (Fig. 2e). According to the above experiments, we conclude that macrophages could kill tumor cells through phagocytizing and secreting soluble factors (including pro-inflammatory cytokines) that can pass the transwell barriers after activation by ROS from light-irradiated TPA-DCR NPs.

ICD can transform tumor cells from being non-immunogenic to immunogenic by releasing damage-associated molecular patterns (DAMPs) that promote antigen identification and uptake, further enhancing the immune response.^{43–46} Taking into account the profound ability of activated M1 macrophages towards killing 4T1 cells, we wondered whether the M1 macrophages that were activated in our strategy could cause the ICD of tumor cells. To answer this question, the DAMPs (ICD markers, *e.g.*, ATP, HMGB1, and HSP70) of 4T1 cells were investigated after being treated with activated M1 macrophages. The 4T1 cells were added to M0 (pre-treated with PBS) and M1 (pre-treated with TPA-DCR NPs + light) macrophages. After 24 h, the ATP in the supernatant and the proteins (HMGB1 and HSP70) in the cell lysate were analyzed by ELISA. Remarkably, the expression levels of secreted ATP from the M1 + 4T1 group were 2-fold higher than those from the M0 + 4T1 group (Fig. 2f). In contrast, the expression levels of HMGB1

(Fig. 2g) and HSP70 (Fig. 2h) in the M1 + 4T1 group were significantly higher than those in the M0 + 4T1 group. Together, these data clearly indicated that M1 macrophages activated with TPA-DCR NPs could induce the ICD of 4T1 tumor cells, which would potentially benefit anti-cancer efficacy *in vivo* for better tumor elimination.

In vivo anti-tumor effect of photodynamic immunotherapy

Encouraged by the findings of our *in vitro* studies, we evaluated the *in vivo* antitumor effect of TPA-DCR NPs in tumor-bearing mice. Firstly, a 4T1 subcutaneous tumor model was established, and the tumor-bearing mice were randomly divided into six groups ($n = 5$) (Fig. 3a). The hypoxic tumor environment was confirmed by immunofluorescence staining, which showed high expression levels of hypoxia-associated protein HIF-1 α in the tumor tissue (Fig. 3b). The mice were intravenously injected with PBS (group i and group ii) or TPA-DCR NPs (groups iii, iv, v, and vi), and the groups ii, iv, vi were treated with light irradiation. To evaluate the role of macrophages in photodynamic immunotherapy, the mice from group v and vi were pre-treated with clodronate liposomes to deplete macrophages 24 h before injecting TPA-DCR NPs. According to *in vivo* fluorescence imaging results (Fig. S18 and S19†), mice were treated with or without white light irradiation at 12 h post injection to maximize the accumulation of NPs in tumor tissues. Tumor volumes were recorded every two days after treatments, demonstrating that the treatment with TPA-DCR NPs + light in group iv could almost completely eliminate the tumors. However, after depleting macrophages, the anti-tumor effect of TPA-DCR NPs in group vi was completely reversed and greatly compromised (Fig. 3c–e). This could be attributed to the fact that the sole ROS generated from PDT could not eliminate all tumor cells in the absence of macrophages, without stimulating the immune response in the tumor microenvironment. Hematoxylin and eosin (H&E) staining results also revealed that the tumor tissues suffered the most damage after treatment with TPA-DCR NPs + light (group iv) (Fig. 3f).

To validate whether the type I photosensitizer of TPA-DCR NPs could reverse the immunosuppression of the hypoxic tumor microenvironment, the populations of M1 and M2 macrophages in tumor tissues were measured by flow cytometry and immunofluorescence staining. Macrophages in tumor tissues were sorted out using magnetic beads at 24 h after PDT treatment. Specific biomarkers were used to individually label M1 (F4/80-APC, CD11c-FITC) and M2 (F4/80-APC, CD206-Alexa 488) macrophages. Results indicated that the number of M1 cells in TPA-DCR NPs + light treatment increased by ~ 3 -fold, and the number of M2 cells decreased by $\sim 42\%$, compared with the PBS group (group i) (Fig. 4a, b, S20 and S21†). In tumor tissues, the expression levels of ICD biomarkers: ATP, HMGB1 and HSP70, showed a significant boost in group iv. Interestingly, the expression levels of ICD biomarkers in mice with macrophage depletion (group vi) were lower than those of group iv (Fig. 4c–e). These findings suggested the importance of TAMs in photodynamic immunotherapy, in which the TPA-DCR NPs could activate TAMs to M1 upon light irradiation to

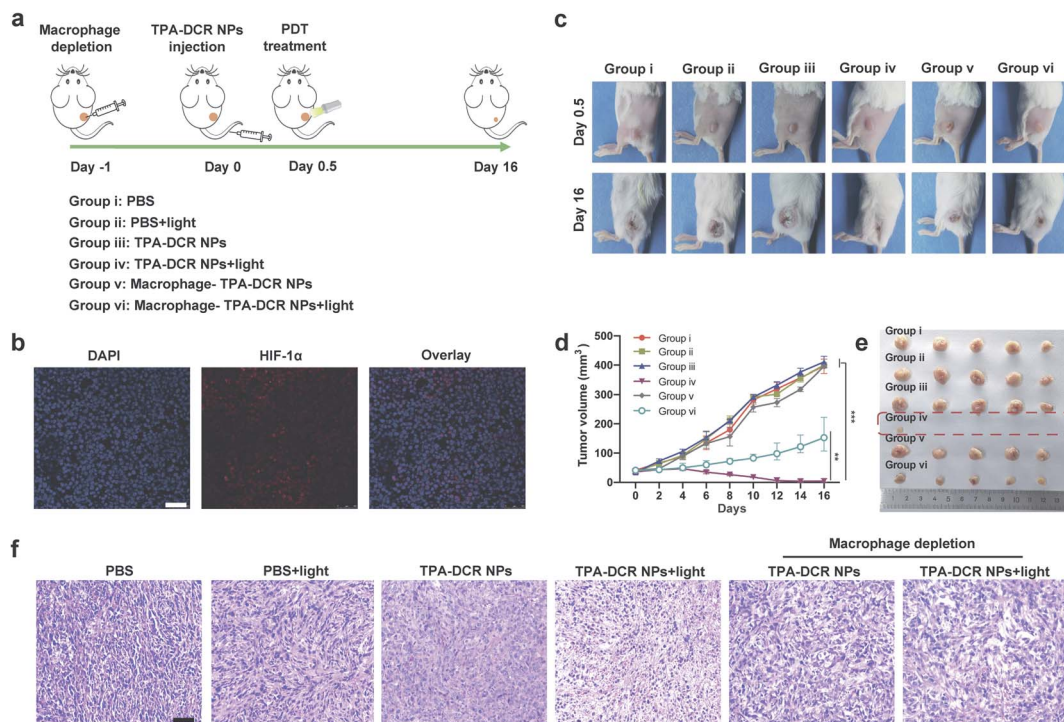


Fig. 3 (a) Schematic illustration of the *in vivo* experimental procedures. The 4T1 tumor-bearing mice were randomly divided into six groups. 1 \times PBS (200 μ L) or TPA-DCR NPs (200 μ L, 1 mg mL⁻¹) were intravenously injected, and the groups ii, iv, vi were treated with light irradiation (300 mW cm⁻², 5 min). In groups v and vi, clodronate liposomes were used to deplete macrophages in tumors. (b) Immunofluorescence imaging of 4T1 tumor sections. Cell nuclei and hypoxia-related protein HIF-1 α were stained with DAPI (blue) and HIF-1 α antibodies (red), respectively. (c) Representative photos of mice from different groups. (d) The tumor growth curves in all groups. (e) Photos of the 4T1 tumors collected from all groups on the 16th day post treatment. (f) Representative H&E staining of tumor tissues from all groups. Scale bar is 100 μ m. ** p < 0.01, *** p < 0.001 vs. group iv, and n = 5.

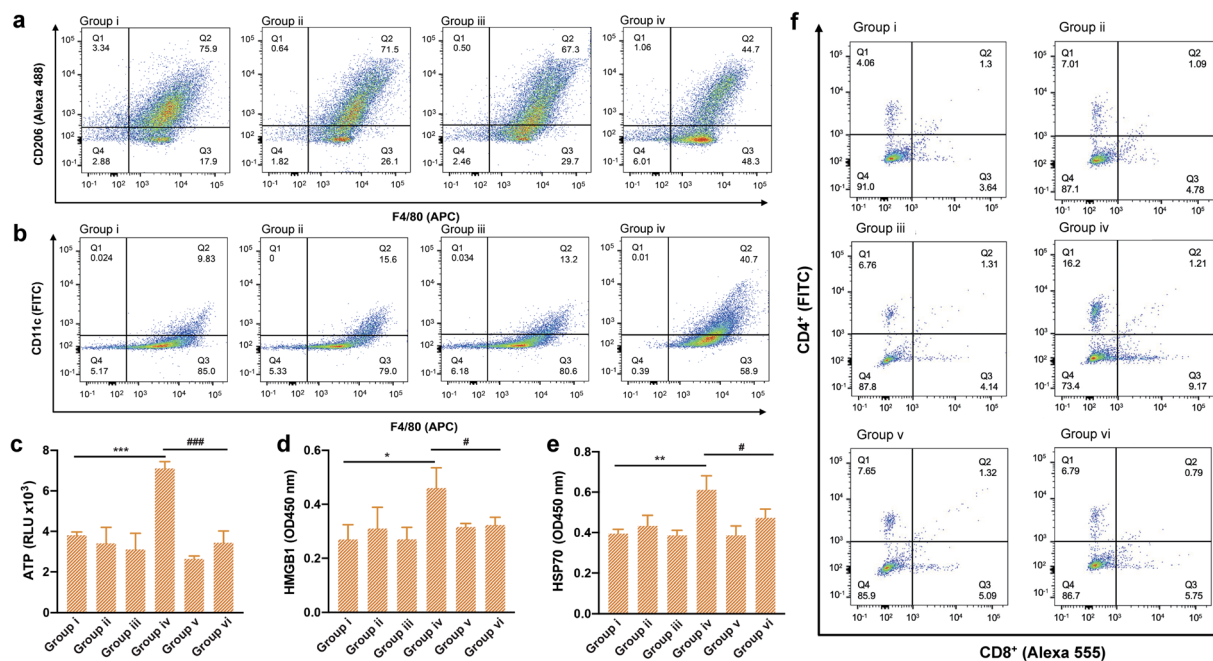
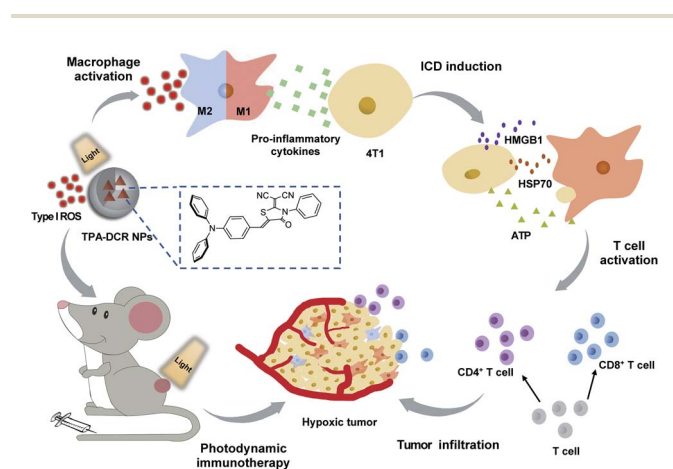


Fig. 4 (a and b) Flow cytometric analysis of the M2 (F4/80, CD206) and M1 (F4/80, CD11c) cells in tumor tissues from groups i to iv. ELISA results showed the expression of (c) ATP, (d) HMGB1 and (e) HSP70 in tumor tissues from different groups, * p < 0.05, ** p < 0.01, *** p < 0.001 vs. the groups i, # p < 0.05, ### p < 0.001 vs. group vi, and n = 3. (f) Flow cytometric analysis of the populations of CD4⁺ and CD8⁺ T cells in tumor tissues collected from different groups.

further induce the ICD of tumor tissues. Considering the importance of T cells in anti-tumor immune response,^{47–49} we also analyzed CD4⁺ T cells and CD8⁺ T cells in tumor tissues and the spleen by immunofluorescence staining and flow cytometry. The results suggested that the numbers of CD4⁺ T cells and CD8⁺ T cells from the spleen in the PDT group (group iv) were ~4-fold and ~3-fold, respectively, compared with those in the control (group i) (Fig. 4f). Meanwhile, the tumor infiltration of CD4⁺ T cells and CD8⁺ T cells also significantly increased by ~3 times after PDT treatment in group iv (Fig. S22 and S23†). According to the literature,^{50–52} such a treatment could significantly inhibit the growth of abscopal tumors and recurrent tumors, when the CD8⁺ T cells and CD4⁺ T cells in the tumor treatment group were ~2–3 times higher than those in the control group. Based on these results, we speculated that type I photosensitizer-triggered macrophage-mediated photodynamic immunotherapy could directly promote the tumor infiltration of T cells by inducing tumor ICD, which could contribute to the profound anti-tumor efficacy and complete tumor ablation without recurrence in the testing period.

In vivo biocompatibility of TPA-DCR NPs

To evaluate the safety of the photosensitizer, we recorded the body weight of the mice during the therapeutic period, and observed no significant difference in all groups (Fig. S24†). The *in vivo* toxicity of TPA-DCR NPs was further evaluated in healthy mice, which were intravenously injected with PBS or TPA-DCR NPs (10 mg kg⁻¹). After 7 days, the morphology of major organs was investigated with H&E staining. No abnormal histology was observed in the heart, liver, spleen, lung or kidney sections from mice that were treated with either PBS or TPA-DCR NPs (Fig. S25†). Furthermore, the results of serum biochemistry (Fig. S26†) and blood routine test of samples from both groups (Fig. S27†) indicated no significant difference in all the key indicators. These results demonstrated the *in vivo* safety of this type I photosensitizer.



Scheme 1 Illustration of using the type I photosensitizer of TPA-DCR NPs for macrophage-mediated photodynamic immunotherapy to treat hypoxic tumors.

Conclusions

In summary, we have rationally synthesized a D–A structured type I photosensitizer of TPA-DCR with aggregation-enhanced ROS generation, and unveiled its working mechanism in photosensitizer-triggered, macrophage-mediated photodynamic immunotherapy (Scheme 1). The type I ROS produced by TPA-DCR NPs could activate the NF- κ B signaling pathway, further promoting the polarization of M0 and M2 macrophages to the M1 state even under hypoxic conditions. Interestingly, unlike the traditional ICD caused by PDT, we discovered that the photosensitizer-polarized M1 macrophages could effectively increase the expression levels of ATP, HMGB1 and HSP70, inducing the ICD of tumor cells, thus enhancing the treatment outcome of photodynamic immunotherapy. Overall, *in vivo* experiments demonstrated that TPA-DCR NPs could reverse the immunosuppressive microenvironment in hypoxic tumors by re-educating TAMs to the M1 phenotype, inducing the ICD of tumor cells, and promoting the tumor infiltration of CD4⁺ and CD8⁺ T cells. Eventually, almost complete tumor elimination has been achieved by single PDT treatment without repeated injection of the photosensitizer or in combination with an immunoadjuvant. Taken together, we demonstrated a strategy of using type I PDT for macrophage activation to overcome the intrinsic hypoxic conditions in tumors and reverse the tumor immunosuppressive environment, shining light on the future development of photodynamic immunotherapy to maximize the potential of the patient's own immune system. Considering that the absorption and emission of TPA-DCR NPs are in the visible region, we will explore a series of type I photosensitizers that can be effectively excited with light sources in the near-infrared region for improved tissue penetration ability, to facilitate their anti-tumor applications in more sophisticated biological studies (*e.g.*, treating deep-seated tumors).

Data availability

The datasets supporting this article have been uploaded as part of the ESI.†

Author contributions

K. L. devised the method and conceived the project. G. Y. designed and performed the experiments, and analyzed the data. S.-B. L. and J.-S. Ni contributed to the chemical experiments. C. L. contributed to the calculation. F. C., M. Z., Y. L., J. G. and T. K. performed the experiments. All authors contributed to writing the manuscript. All authors have given approval to the final version of the manuscript.

Conflicts of interest

There are no conflicts to declare.

Acknowledgements

All animal experiments were performed in strict accordance with the guidelines for the Care and Use of Laboratory Animals of

SUSTech and approved by the Animal Ethics Committee of the Center for Experimental Animal Research of SUSTech (SUSTC-2018-115), China. The authors are grateful to the Ministry of Science and Technology of China (2020YFA0908900), the National Natural Science Foundation of China (31870991), the Department of Science and Technology of Guangdong Province (2019ZT08Y191), the Shenzhen Key Laboratory of Smart Healthcare Engineering (ZDSYS2020081144003009), and the Shenzhen Science and Technology Program (JSGG20200225151916021, KQTD20190929172743294, and JCYJ20190809154011696) for financial support. The time-resolved fluorescence characterization was supported by the Shenzhen Key Laboratory of Full Spectral Solar Electricity Generation (FSSEG) from the Shenzhen Key Laboratory Project (No. ZDSYS201602261933302). The authors thank Dr Yang Y., Ren Z., Li H. and Lin L. at the SUSTech Core Research Facilities for the EPR and HRMS testing, respectively. The authors acknowledge the Center for Computational Science and Engineering at SUSTech for theoretical calculation support and SUSTech Core Research Facilities for technical support. All *in vivo* procedures have been approved by the Animal Ethics Committee of the Center for Experimental Animal Research of SUSTech, China.

References

- 1 B. Ding, S. Shao, C. Yu, B. Teng, M. Wang, Z. Cheng, K.-L. Wong, P. a. Ma and J. Lin, *Adv. Mater.*, 2018, **30**, 1900927.
- 2 H.-T. Feng, Y. Li, X. Duan, X. Wang, C. Qi, J. W. Y. Lam, D. Ding and B. Z. Tang, *J. Am. Chem. Soc.*, 2020, **142**, 15966–15974.
- 3 A. Gao, B. Chen, J. Gao, F. Zhou, M. Saeed, B. Hou, Y. Li and H. Yu, *Nano Lett.*, 2020, **20**, 353–362.
- 4 H. Zhu, Y. Fang, Q. Miao, X. Qi, D. Ding, P. Chen and K. Pu, *ACS Nano*, 2017, **11**, 8998–9009.
- 5 S. He, J. Li, Y. Lyu, J. Huang and K. Pu, *J. Am. Chem. Soc.*, 2020, **142**, 7075–7082.
- 6 P. Cheng, J. Zhang, J. Huang, Q. Miao, C. Xu and K. Pu, *Chem. Sci.*, 2018, **9**, 6340–6347.
- 7 J. Li, Y. Fang, Y. Zhang, H. Wang, Z. Yang and D. Ding, *Adv. Mater.*, 2021, **33**, 2008518.
- 8 D.-W. Zheng, F. Gao, Q. Cheng, P. Bao, X. Dong, J.-X. Fan, W. Song, X. Zeng, S.-X. Cheng and X.-Z. Zhang, *Nat. Commun.*, 2020, **11**, 1985.
- 9 A. A. Barkal, K. Weiskopf, K. S. Kao, S. R. Gordon, B. Rosental, Y. Y. Yiu, B. M. George, M. Markovic, N. G. Ring, J. M. Tsai, K. M. McKenna, P. Y. Ho, R. Z. Cheng, J. Y. Chen, L. J. Barkal, A. M. Ring, I. L. Weissman and R. L. Maute, *Nat. Immunol.*, 2018, **19**, 76–84.
- 10 Z. Gu, T. Liu, J. Tang, Y. Yang, H. Song, Z. K. Tuong, J. Fu and C. Yu, *J. Am. Chem. Soc.*, 2019, **141**, 6122–6126.
- 11 J.-J. Hu, Q. Lei and X.-Z. Zhang, *Prog. Mater. Sci.*, 2020, **114**, 100685.
- 12 Q. Hu, H. Li, E. Archibong, Q. Chen, H. Ruan, S. Ahn, E. Dukhovlina, Y. Kang, D. Wen, G. Dotti and Z. Gu, *Nat. Biomed. Eng.*, 2021, **5**, 1038–1047.
- 13 J. Li, X. Jiang, H. Li, M. Gelinsky and Z. Gu, *Adv. Mater.*, 2021, **33**, 2004172.
- 14 H. Ruan, Q. Hu, D. Wen, Q. Chen, G. Chen, Y. Lu, J. Wang, H. Cheng, W. Lu and Z. Gu, *Adv. Mater.*, 2019, **31**, 1970120.
- 15 L. Li, C. Shao, T. Liu, Z. Chao, H. Chen, F. Xiao, H. He, Z. Wei, Y. Zhu, H. Wang, X. Zhang, Y. Wen, B. Yang, F. He and L. Tian, *Adv. Mater.*, 2020, **32**, 2003471.
- 16 J. Sun, K. Du, J. Diao, X. Cai, F. Feng and S. Wang, *Angew. Chem., Int. Ed.*, 2020, **59**, 12122–12128.
- 17 H. Zhu, J. Li, X. Qi, P. Chen and K. Pu, *Nano Lett.*, 2018, **18**, 586–594.
- 18 M.-Z. Zou, W.-L. Liu, H.-S. Chen, X.-F. Bai, F. Gao, J.-J. Ye, H. Cheng and X.-Z. Zhang, *Natl. Sci. Rev.*, 2021, **8**, nwa160.
- 19 Z. Liu, H. Zou, Z. Zhao, P. Zhang, G.-G. Shan, R. T. K. Kwok, J. W. Y. Lam, L. Zheng and B. Z. Tang, *ACS Nano*, 2019, **13**, 11283–11293.
- 20 Q. Y. Li, J. Y. Gong, Y. Li, R. Y. Zhang, H. R. Wang, J. W. Y. Lam, H. H. Y. Sung, I. D. Williams, R. T. K. Kwok, M.-H. Li, J. G. Wang and B. Z. Tang, *Chem. Sci.*, 2021, **12**, 709–717.
- 21 M. Wu, X. Liu, H. Chen, Y. Duan, J. Liu, Y. Pan and B. Liu, *Angew. Chem., Int. Ed.*, 2021, **60**, 9093–9098.
- 22 M. Kang, Z. Zhang, N. Song, M. Li, P. Sun, X. Chen, D. Wang and B. Z. Tang, *Aggregate*, 2020, **1**, 80–106.
- 23 C. Ji, L. Lai, P. Li, Z. Wu, W. Cheng and M. Yin, *Aggregate*, 2020, **2**, e114.
- 24 J.-S. Ni, T. Min, Y. Li, M. Zha, P. Zhang, C. L. Ho and K. Li, *Angew. Chem., Int. Ed.*, 2020, **59**, 10179–10185.
- 25 M. Oszejca, M. Brindell, L. Orzel, J. M. Dabrowski, K. Spiewak, P. Labuz, M. Pacia, A. Stochel-Gaudyn, W. Macyk, R. van Eldik and G. Stochel, *Coord. Chem. Rev.*, 2016, **327–328**, 143–165.
- 26 Y.-Y. Wang, Y.-C. Liu, H. Sun and D.-S. Guo, *Coord. Chem. Rev.*, 2019, **395**, 46–62.
- 27 Z. Zhou, J. Song, L. Nie and X. Chen, *Chem. Soc. Rev.*, 2016, **45**, 6597–6626.
- 28 M. C. DeRosa and R. J. Crutchley, *Coord. Chem. Rev.*, 2002, **233–234**, 351–371.
- 29 D. Wang, H. Su, R. T. K. Kwok, X. Hu, H. Zou, Q. Luo, M. M. S. Lee, W. Xu, J. W. Y. Lam and B. Z. Tang, *Chem. Sci.*, 2018, **9**, 3685–3693.
- 30 Z. Lv, H. Wei, Q. Li, X. Su, S. Liu, K. Y. Zhang, W. Lv, Q. Zhao, X. Li and W. Huang, *Chem. Sci.*, 2018, **9**, 502–512.
- 31 Y. Zheng, H. Lu, Z. Jiang, Y. Guan, J. Zou, X. Wang, R. Cheng and H. Gao, *J. Mater. Chem. B*, 2017, **5**, 6277–6281.
- 32 M. J. Frisch, G. W. Trucks, H. B. Schlegel, G. E. Scuseria, M. A. Robb, J. R. Cheeseman, G. Scalmani, V. Barone, G. A. Petersson, H. Nakatsuji, X. Li, M. Caricato, A. V. Marenich, J. Bloino, B. G. Janesko, R. Gomperts, B. Mennucci, H. P. Hratchian, J. V. Ortiz, A. F. Izmaylov and J. L. Sonnenberg, *et al.*, *Gaussian 16, Revision B.01*, Gaussian, Inc., Wallingford CT, 2016.
- 33 W. Wu, D. Mao, S. Xu, Kenry, F. Hu, X. Li, D. Kong and B. Liu, *Chem*, 2018, **4**, 1937–1951.
- 34 K.-X. Teng, W.-K. Chen, L.-Y. Niu, W.-H. Fang, G. Cui and Q.-Z. Yang, *Angew. Chem., Int. Ed.*, 2021, **60**, 19912–19920.

- 35 J.-S. Ni, X. Zhang, G. Yang, T. Kang, X. Lin, M. Zha, Y. Li, L. Wang and K. Li, *Angew. Chem., Int. Ed.*, 2020, **59**, 11298–11302.
- 36 G. Weber and F. W. J. Teale, *Trans. Faraday Soc.*, 1957, **53**, 646–655.
- 37 M. Nemoto, H. Kokubun and M. Koizumi, *Bull. Chem. Soc. Jpn.*, 1969, **42**, 1223–1230.
- 38 X. He, Y. Yang, Y. Guo, S. Lu, Y. Du, J.-J. Li, X. Zhang, N. L. C. Leung, Z. Zhao, G. Niu, S. Yang, Z. Weng, R. T. K. Kwok, J. W. Y. Lam, G. Xie and B. Z. Tang, *J. Am. Chem. Soc.*, 2020, **142**, 3959–3969.
- 39 G. Yang, J.-S. Ni, Y. Li, M. Zha, Y. Tu and K. Li, *Angew. Chem., Int. Ed.*, 2021, **60**, 5386–5393.
- 40 Y. Cheng, X. Kong, Y. Chang, Y. Feng, R. Zheng, X. Wu, K. Xu, X. Gao and H. Zhang, *Adv. Mater.*, 2020, **32**, 1908109.
- 41 G. Yang, S. Z. F. Phua, W. Q. Lim, R. Zhang, L. Feng, G. Liu, H. Wu, A. K. Bindra, D. Jana, Z. Liu and Y. Zhao, *Adv. Mater.*, 2019, **31**, 1901513.
- 42 K. Li, Z. Zhu, P. Cai, R. Liu, N. Tomczak, D. Ding, J. Liu, W. Qin, Z. Zhao, Y. Hu, X. Chen, B. Z. Tang and B. Liu, *Chem. Mater.*, 2013, **25**, 4181–4187.
- 43 C. Chen, X. Ni, S. Jia, Y. Liang, X. Wu, D. Kong and D. Ding, *Adv. Mater.*, 2019, **31**, 1904914.
- 44 B. Hou, L. Zhou, H. Wang, M. Saeed, D. Wang, Z. Xu, Y. Li and H. Yu, *Adv. Mater.*, 2020, **32**, 1907210.
- 45 J. Li, H. Gao, R. Liu, C. Chen, S. Zeng, Q. Liu and D. Ding, *Sci. China: Chem.*, 2020, **63**, 1428–1434.
- 46 L. Sun, F. Shen, L. Tian, H. Tao, Z. Xiong, J. Xu and Z. Liu, *Adv. Mater.*, 2021, **33**, 2007910.
- 47 J. Xu, L. Xu, C. Wang, R. Yang, Q. Zhuang, X. Han, Z. Dong, W. Zhu, R. Peng and Z. Liu, *ACS Nano*, 2017, **11**, 4463–4474.
- 48 C. Wang, Y. Ye, Q. Hu, A. Bellotti and Z. Gu, *Adv. Mater.*, 2017, **29**, 1606036.
- 49 C. Zhang, F. Gao, W. Wu, W.-X. Qiu, L. Zhang, R. Li, Z.-N. Zhuang, W. Yu, H. Cheng and X.-Z. Zhang, *ACS Nano*, 2019, **13**, 11249–11262.
- 50 B. Hou, L. Zhou, H. Wang, M. Saeed, D. Wang, Z. Xu, Y. Li and H. Yu, *Adv. Mater.*, 2020, **32**, 1907210.
- 51 J. Xu, B. Zheng, S. Zhang, X. Liao, Q. Tong, G. Wei, S. Yu, G. Chen, A. Wu, S. Gao, Y. Qian, Z. Xiao and W. Lu, *Adv. Funct. Mater.*, 2021, **31**, 2008022.
- 52 Y. Wang, Z. Wang, B. Chen, Q. Yin, M. Pan, H. Xia, B. Zhang, Y. Yan, Z. Jiang, Q. Zhang and Y. Wang, *Nano Lett.*, 2021, **21**, 4371–4380.